



Title	Wavelength-selective spin-current generator using infrared plasmonic metamaterials
Author(s)	Ishii, Satoshi; Uchida, Ken-ichi; Dao, Thang Duy; Wada, Yoshiki; Saitoh, Eiji; Nagao, Tadaaki
Citation	APL Photonics, 2(10), 106103 <a href="https://doi.org/10.1063/1.4991438">https://doi.org/10.1063/1.4991438</a>
Issue Date	2017-10
Doc URL	<a href="http://hdl.handle.net/2115/72111">http://hdl.handle.net/2115/72111</a>
Rights	Copyright 2017 Author(s). This article is distributed under a Creative Commons Attribution (CC BY) License.
Rights(URL)	<a href="https://creativecommons.org/licenses/by/4.0/">https://creativecommons.org/licenses/by/4.0/</a>
Type	article
Additional Information	There are other files related to this item in HUSCAP. Check the above URL.
File Information	APL photonics2-10_106103.pdf



[Instructions for use](#)

## Wavelength-selective spin-current generator using infrared plasmonic metamaterials

Satoshi Ishii, Ken-ichi Uchida, Thang Duy Dao, Yoshiki Wada, Eiji Saitoh, and Tadaaki Nagao

Citation: *APL Photonics* **2**, 106103 (2017); doi: 10.1063/1.4991438

View online: <https://doi.org/10.1063/1.4991438>

View Table of Contents: <http://aip.scitation.org/toc/app/2/10>

Published by the [American Institute of Physics](#)

---

### Articles you may be interested in

[Nonreciprocity and one-way topological transitions in hyperbolic metamaterials](#)

*APL Photonics* **2**, 076103 (2017); 10.1063/1.4985064

[Negative force on free carriers in positive index nanoparticles](#)

*APL Photonics* **2**, 101301 (2017); 10.1063/1.4991567

[Direct laser written polymer waveguides with out of plane couplers for optical chips](#)

*APL Photonics* **2**, 106102 (2017); 10.1063/1.4994806

[Split-disk micro-lasers: Tunable whispering gallery mode cavities](#)

*APL Photonics* **2**, 096103 (2017); 10.1063/1.4985766

[Ultra-high Q/V hybrid cavity for strong light-matter interaction](#)

*APL Photonics* **2**, 086101 (2017); 10.1063/1.4994056

[Terahertz particle-in-liquid sensing with spoof surface plasmon polariton waveguides](#)

*APL Photonics* **2**, 116102 (2017); 10.1063/1.4998566

---

**AIP** | Conference Proceedings

Get **30% off** all  
print proceedings!

Enter Promotion Code **PDF30** at checkout



## Wavelength-selective spin-current generator using infrared plasmonic metamaterials

Satoshi Ishii,<sup>1,a,b</sup> Ken-ichi Uchida,<sup>2,3,4,5,a,c</sup> Thang Duy Dao,<sup>1</sup> Yoshiki Wada,<sup>6</sup> Eiji Saitoh,<sup>3,4,7,8</sup> and Tadaaki Nagao<sup>1,9</sup>

<sup>1</sup>International Center for Materials Nanoarchitectonics (WPI-MANA), National Institute for Materials Science (NIMS), Tsukuba, Ibaraki 305-0044, Japan

<sup>2</sup>Research Center for Magnetic and Spintronic Materials, National Institute for Materials Science (NIMS), Tsukuba, Ibaraki 305-0047, Japan

<sup>3</sup>Institute for Materials Research, Tohoku University, Sendai, Miyagi 980-8577, Japan

<sup>4</sup>Center for Spintronics Research Network, Tohoku University, Sendai, Miyagi 980-8577, Japan

<sup>5</sup>PRESTO, Japan Science and Technology Agency, Saitama 332-0012, Japan

<sup>6</sup>Research Center for Functional Materials, National Institute for Materials Science (NIMS), Tsukuba, Ibaraki 305-0044, Japan

<sup>7</sup>Advanced Institute for Materials Research, Tohoku University, Sendai, Miyagi 980-8577, Japan

<sup>8</sup>Advanced Science Research Center, Japan Atomic Energy Agency, Tokai, Ibaraki 319-1195, Japan

<sup>9</sup>Department of Condensed Matter Physics, Graduate School of Science, Hokkaido University, Sapporo, Hokkaido 060-0810, Japan

(Received 21 June 2017; accepted 11 September 2017; published online 10 October 2017)

A subwavelength plasmonic absorber is an ideal platform for absorbing light locally at a desired wavelength. Here, we demonstrate wavelength-selective spin current generation by combining plasmonic absorbers with Pt/yttrium-iron-garnet spintronic devices. These devices are widely used for investigating spin-current phenomena, such as the spin Seebeck effect. At the resonance of the plasmonic absorber in the mid-infrared regime, enhanced spin-current signals are recorded. The observed light-induced spin current can be attributed to both the spin Seebeck effect and photo-spin-voltaic effect. Our results open new prospects for using plasmonic absorbers to bridge nanophotonics and spintronics in numbers of opto-spintronic applications. © 2017 Author(s). All article content, except where otherwise noted, is licensed under a Creative Commons Attribution (CC BY) license (<http://creativecommons.org/licenses/by/4.0/>). <https://doi.org/10.1063/1.4991438>

### I. INTRODUCTION

Spintronics and photonics show great promise for the development of post electronics technologies, and their combination in a single device may yet yield significant benefit. Several studies have pioneered the conversion of light into electron spin.<sup>1–5</sup> Because spintronics deals with the spin of electrons, most of the past studies have used circularly polarized light and semiconductors to generate a spin current, i.e., a flow of spin angular momentum that drives various spintronic functions.<sup>6</sup> A novel effect was recently reported, whereby a spin current is generated by un-polarized light, which is the photo-spin-voltaic (PSV) effect.<sup>7</sup> In the PSV process, the spin current is generated directly from the absorbed photons in a paramagnetic metal film [typically, platinum (Pt)] placed over a magnetic insulator [typically, yttrium iron garnet (YIG)]. The light-induced spin current is in turn converted into an electric voltage by the inverse spin Hall effect (ISHE)<sup>8–12</sup> when the spin-orbit interaction of the paramagnetic film is strong.

<sup>a</sup>S. Ishii and K. Uchida contributed equally to this work.

<sup>b</sup>E-mail: [sishii@nims.go.jp](mailto:sishii@nims.go.jp)

<sup>c</sup>E-mail: [UCHIDA.Kenichi@nims.go.jp](mailto:UCHIDA.Kenichi@nims.go.jp)

Another process for generating a spin current from light involves a more indirect process. Light generates heat when it is absorbed by a metallic film on a magnetic insulator. The resulting thermal gradient across the film can be the source of the spin Seebeck effect (SSE) when a magnetic field is applied perpendicular to the thermal gradient.<sup>13,14</sup> Since the SSE can also generate a voltage through the ISHE, it has been recognized as an alternative approach for generating electricity from light sources.<sup>15–19</sup>

Efficient light confinement and absorption are critically important for achieving an efficient light-to-spin conversion. For this reason, plasmonic metamaterials provide ideal subwavelength platforms for controlling light flow with complete flexibility. In particular, plasmonic absorbers have generated considerable interest. Because light is confined in the subwavelength regime in a plasmonic absorber, electromagnetic fields are strongly enhanced before the light is absorbed. Absorption can be almost unity in a narrow wavelength range at plasmon resonances. The absorption bands can be tuned arbitrarily by adjusting the geometry, in terms of either the film thickness or the size of the nanostructure. After pioneering work carried out in the late 2000s,<sup>20–22</sup> various plasmonic absorbers have been demonstrated, operating from the visible<sup>23</sup> to mid-infrared (mid-IR)<sup>24–26</sup> regimes, in applications that include carbohydrates<sup>22</sup> and molecular<sup>27,28</sup> sensing, photodetectors<sup>29</sup> and selective thermal emitters.<sup>30–32</sup>

Those previous studies exploited the wavelength-selective absorptivity (in turn, emissivity) in plasmonic absorbers. It is important to appreciate that, when irradiated at the resonance wavelength, the light absorbed by a plasmonic absorber eventually heats the sample. Subwavelength thickness and planar geometry together with near unity absorptivity, therefore make plasmonic absorbers an ideal structure to be integrated to a device responding to heat such as pyroelectric mid-IR sensors.<sup>33</sup>

In the present work, we experimentally demonstrated the generation of a spin current by a plasmonic metamaterial. Owing to the wavelength-selective property of the plasmonic absorber, a spin-current-induced voltage was enhanced at the resonance wavelength. We first performed multiphysics simulations based on a finite element method to calculate the electromagnetic response as well as the temperature increase due to the mid-IR light absorption of the plasmonic absorber. For the experiments, we fabricated a plasmonic absorber on the top of a Pt/YIG spintronic device to investigate light-to-spin conversion. A distinct ISHE voltage ( $V_{\text{ISHE}}$ ) generated by the PSV effect and the longitudinal SSE (LSSE) was observed at the resonance wavelength in the mid-IR regime. Our device can be readily developed into a wavelength-selective IR sensor, thereby opening a wide range of research avenues in photo-induced spin-current phenomena as well as in energy harvesting.

## II. SAMPLE DESIGN AND NUMERICAL SIMULATIONS

### A. Sample structure and working principle

The basic concept of the device is outlined in Fig. 1. The upper part of the device is a plasmonic absorber that is a metal-insulator-metal (MIM) hybrid structure, where the metal in the uppermost layer is in the form of a hexagonal array of metallic disks. The lower part forms a typical structure used to generate a spin current by the PSV effect and the LSSE, where a metal film is deposited onto a magnetic insulator. In the current case, the metal film also serves as the bottom metal film of the MIM plasmonic absorber. This sample differs from that used in a previous study<sup>34</sup> in which random plasmonic nanoparticles were embedded in a magnetic insulator.

The working principle of our device is as follows: When light is incident onto the sample at the specific wavelength determined by the geometrical parameters of the MIM structure, the plasmonic absorber exhibits a strong plasmonic resonance which maximizes the absorption. A fraction of the absorbed light partially triggers the PSV effect, while the remaining fraction heats up the sample, thus generating a thermal gradient across the thickness ( $z$  direction). This thermal gradient then derives the LSSE in the lower part of the sample. In the LSSE, a thermal gradient directed perpendicular to the interface of a magnetic insulator (e.g., YIG,  $\text{Fe}_3\text{O}_4$ , and  $\text{BaFe}_{12}\text{O}_{19}$ ) and a metal film (e.g., Pt, Au, W, Ta, and NiFe) excites magnons in the insulator.<sup>35</sup> The non-equilibrium magnons generate a spin

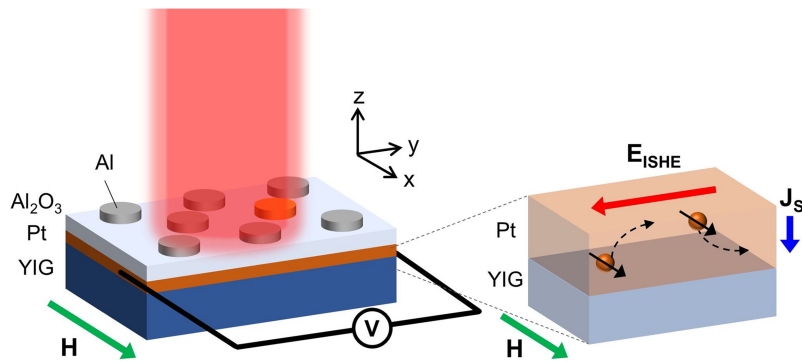


FIG. 1. Schematic of the sample and detection scheme for photo- (plasmon-) induced voltage generation, where  $\mathbf{H}$ , and  $\mathbf{J}_S$ , and  $\mathbf{E}_{\text{ISHE}}$  represent the external magnetic field, the spatial direction of the spin current, and electric field induced by the ISHE, respectively.  $|\mathbf{E}_{\text{ISHE}}|$  is proportional to light induced ISHE voltage ( $V_{\text{ISHE}}$ ).

current ( $\mathbf{J}_S$ ) in the metal layer in the direction parallel to the thermal gradient. Finally, the excited spin current is converted into an electric voltage along the  $y$  direction by the ISHE in the metal layer, when the magnetic field ( $\mathbf{H}$ ) is applied along the  $x$  direction.

In short, owing to the plasmonic absorber, the device allows the electrical detection of a specific wavelength through the PSV effect and the LSSE. Note that the simultaneous detection of the PSV effect and the LSSE has been reported for planar Pt/YIG samples but without arbitrary wavelength tuning.<sup>7</sup> The same general concept can be applied to any other wavelength range, though the present device is particularly designed to target the mid-IR range. In contrast to the previous work where plasmon resonances in random Au nanoparticles in the visible region generate a spin current,<sup>34</sup> our device is the first to combine mid-IR plasmonic metamaterials with spintronic devices, which enables stronger light absorption and an excellent tunability of their resonance wavelengths.

## B. Numerical simulations

In the numerical calculations as well as in the experiments, the materials used were aluminum (Al), alumina ( $\text{Al}_2\text{O}_3$ ), Pt, and YIG ordered from top to bottom (see Fig. 1). The thicknesses of the Al,  $\text{Al}_2\text{O}_3$ , Pt, and YIG are 100 nm, 200 or 250 nm, 10 nm, and 112  $\mu\text{m}$ , respectively. In experiment, single-crystalline YIG layers were fabricated on a 0.4-mm-thick double-side-polished  $\text{Gd}_3\text{Ga}_3\text{O}_{12}$  (GGG) substrate by liquid phase epitaxy. By this process, the YIG layers were formed on the both side of the GGG. The size of the YIG/GGG/YIG substrate was  $7 \times 3 \text{ mm}^2$ . Three samples with different Al disk sizes were fabricated named as A1, A2, and A3. As a control sample, a sample without periodic Al disks and  $\text{Al}_2\text{O}_3$  was also prepared and labeled as A0. The parameters of the four samples are tabulated in Table S1 of the [supplementary material](#). All the geometrical and material parameters of the fabricated samples were used in the numerical calculations as described below.

We first present the numerical studies designed to understand the optical and thermal properties of the devices. The numerical simulation couples Maxwell's equations and heat transfer equation, such that the absorbed electromagnetic energy becomes the heat source in heat transfer calculation. This multiphysics problem was solved using a finite-element method implemented with a commercial package (COMSOL Multiphysics). The mid-IR permittivities of the materials except Al used in the electromagnetic simulation were extracted from spectroscopic ellipsometry measurement using Sentech SENDIRA, as summarized in Fig. S1 of the [supplementary material](#). The permittivity of Al was taken from Ref. 36. The densities, thermal conductivities, and heat capacitances at constant pressure were taken from the literature<sup>37</sup> to perform the heat transfer simulation. The details of the simulation settings are provided in Sec. S1 of the [supplementary material](#).

The results of the multiphysics simulations excited at monochromatic 10 mW mi-IR light are summarized in Fig. 2. Figure 2(a) plots the sum of the absorptivity in the Pt film and Al disk (except for sample A0). Each sample shows a clear absorption peak corresponding to the plasmonic resonances. The peak position shifts to longer wavelengths as the Al disk size increases. In contrast, the curve

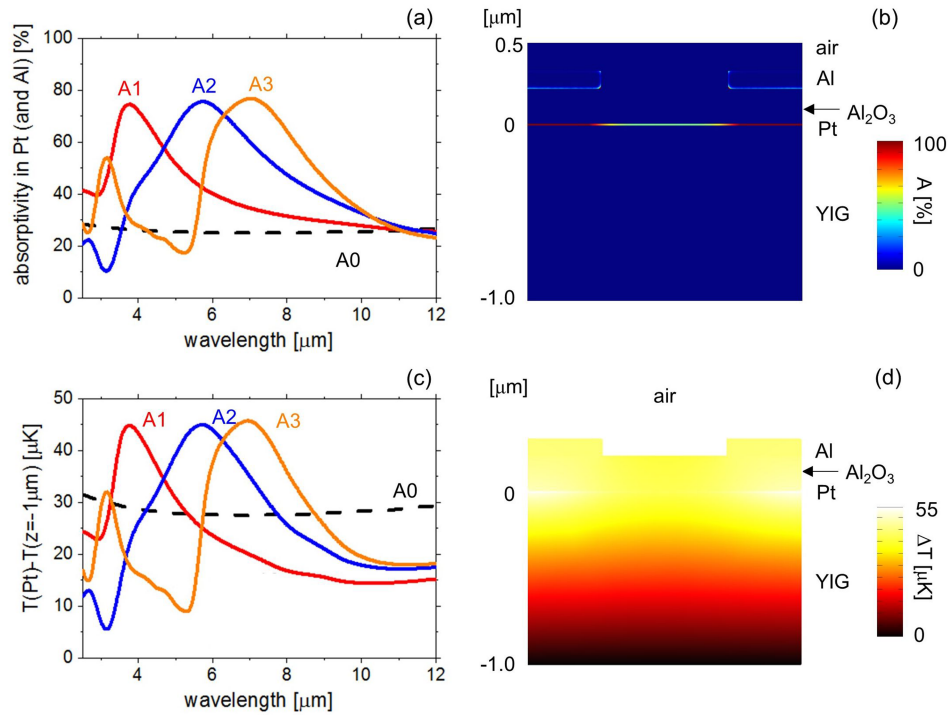


FIG. 2. (a) Sum of the absorptivities in the Pt and Al layers as determined by numerical simulations. The curve referring to sample A0 represents the absorptivity in the Pt only. (b) Cross-sectional absorptivity of sample A1 at the plasmon resonance wavelength of  $3.75 \mu\text{m}$ . (c) Simulated temperature difference between the Pt film and the YIG layer. The temperature in YIG was determined  $1 \mu\text{m}$  below the Pt film. (d) Cross-sectional temperature distribution in sample A1 at the wavelength of  $3.75 \mu\text{m}$ .

corresponding to A0 is featureless. These results indicate that the MIM disk structures function as wavelength-selective absorbers. As an example, Fig. 2(b) shows the cross sectional absorption of sample A1 at  $3.75 \mu\text{m}$ , corresponding to the plasmon resonance. Even though the Pt film is located below the Al disks and the  $\text{Al}_2\text{O}_3$  layer, the absorptivity in the Pt film is the strongest absorption among all the materials considered. This is a significant advantage for concentrating heat and hence inducing a thermal gradient efficiently.

Figure 2(c) shows the difference between the average temperature of the Pt film and the temperature of YIG  $1 \mu\text{m}$  below the Pt film as a function of the wavelength of the incident light. The peak locations of the temperature differences for samples A1–A3 correspond to the peak locations of the absorptivities shown in Fig. 2(a). It is noteworthy that the temperature difference for sample A0 is greater than those for samples A1–A3 away from the resonances. Figure 2(d) maps the cross-sectional temperature profile of sample A1 at  $3.75 \mu\text{m}$ . As can be expected from Fig. 2(b), the temperature is maximum in the Pt film and decreases along the thickness direction. The simulation suggests that the thermal gradient along this direction can induce the LSSE, as confirmed in experiments.

Whereas the multiphysics simulations presented in Fig. 2 refer to infinitely large structures by imposing periodic boundary conditions, next we also performed simulations by considering the actual sample sizes. In order to do so, the simulation process was split into two steps: we first simulate the absorptivities of the samples in electromagnetic module for a unit cell and then use the calculated absorptivities to simulate the temperature in the whole sample. A temperature profile for sample A1 at  $3.75 \mu\text{m}$  is shown in Fig. 3(a), and the simulated temperature differences between the Pt film and the YIG layer are plotted in Fig. 3(b). The central part of the sample is uniformly heated by the light irradiation, and the temperature differences are qualitatively similar to the results shown in Fig. 2(c). Hence, Fig. 3 verifies that the assumption of an infinite periodicity was reasonable for the purpose of estimating the temperature profiles in the experiments.

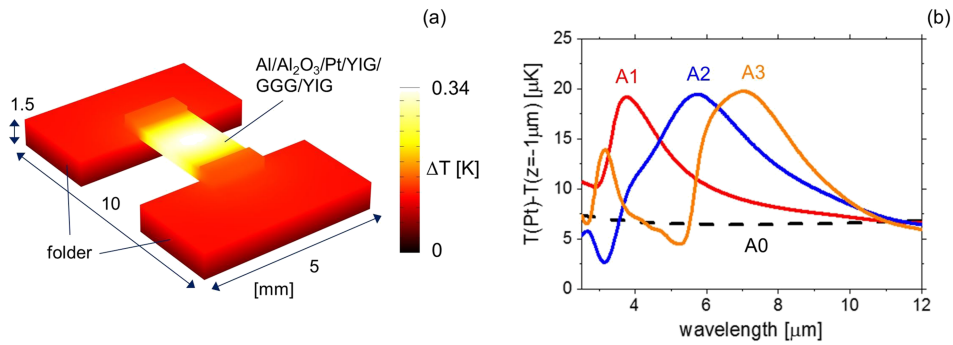


FIG. 3. (a) Simulated temperature increase for sample A1 where the illumination is at 10 mW at the resonance wavelength of  $3.75 \mu\text{m}$ . The incident Gaussian beam diameter is 4 mm. (b) Simulated temperature difference between the Pt film and YIG as a function of the wavelength at 10 mW. The YIG temperatures were taken at the depth of  $1 \mu\text{m}$  below the Pt film, and the average temperature of the Pt film was used to calculate the temperature difference.

### III. EXPERIMENT AND RESULTS

Following the numerical studies, we experimentally demonstrated the generation of optically and thermally induced spin current by the ISHE. To fabricate the samples, double-side polished GGG having YIG layers on the both sides were used as substrates. The fabrication of the upper MIM disk structure follows the combination of colloidal lithography and reactive ion etching (RIE) processes as reported in the literature.<sup>31</sup> Briefly, after the RF sputtering of a Pt film on the YIG,  $\text{Al}_2\text{O}_3$  and Al films were subsequently sputtered except for sample A0. Next, the Al film was covered by a monolayer of polystyrene (PS) (Polybead polystyrene microspheres, Polysciences) microspheres. Then the sample was etched by the RIE processes twice; first with an oxygen plasma and second with a mixture of  $\text{BCl}_3$  and chlorine gases. The etching time for the oxygen plasma determined the size of the PS spheres and hence the Al disk size lying underneath. Finally, the remaining PS microspheres were removed by sonication in toluene.

Figure 4 shows field-emission scanning electron microscope (FE-SEM, SU8200, Hitachi) images of the three samples with the MIM disk arrays seem from above. Since the PS microspheres form closely packed hexagonal lattice, the Al disks also display a hexagonal periodicity.

The reflectivities of the samples were measured using a Fourier Transform Infrared (FTIR) spectroscopy apparatus (Nicolet iS50, Thermo Scientific) and are plotted in Fig. 5(a). Except for sample A0, the reflectivity of each sample shows a minimum around the plasmon resonance. As the Al disk becomes larger, the resonance wavelength increases, in qualitative agreement with the full-wave numerical simulations also presented in Fig. 5(a). Some of the discrepancies between the measured and simulated reflectivities could be due to the surface roughness or imperfect shapes of the disks, neither of which was modeled in the simulations.

In the measurement of the ISHE voltage generated by the light-induced spin current, we used a wavelength tunable IR laser. The laser system consists of a Ti:Sapphire regenerative amplifier (Solstice, Spectra-Physics) and a non-collinear difference frequency generator (NDFG, Light Conversion) connected to an optical parametric oscillator (TOPAS Prime, Spectra-Physics). The average

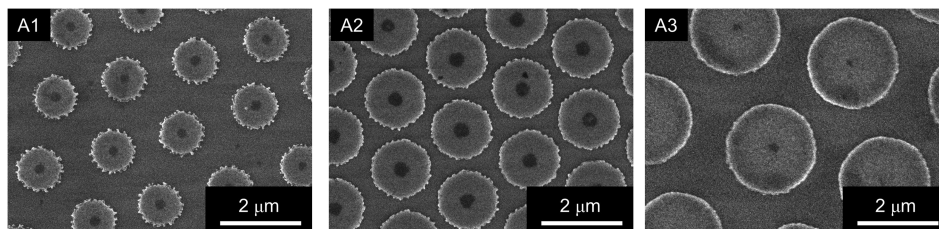


FIG. 4. FE-SEM images of samples A1, A2, and A3.

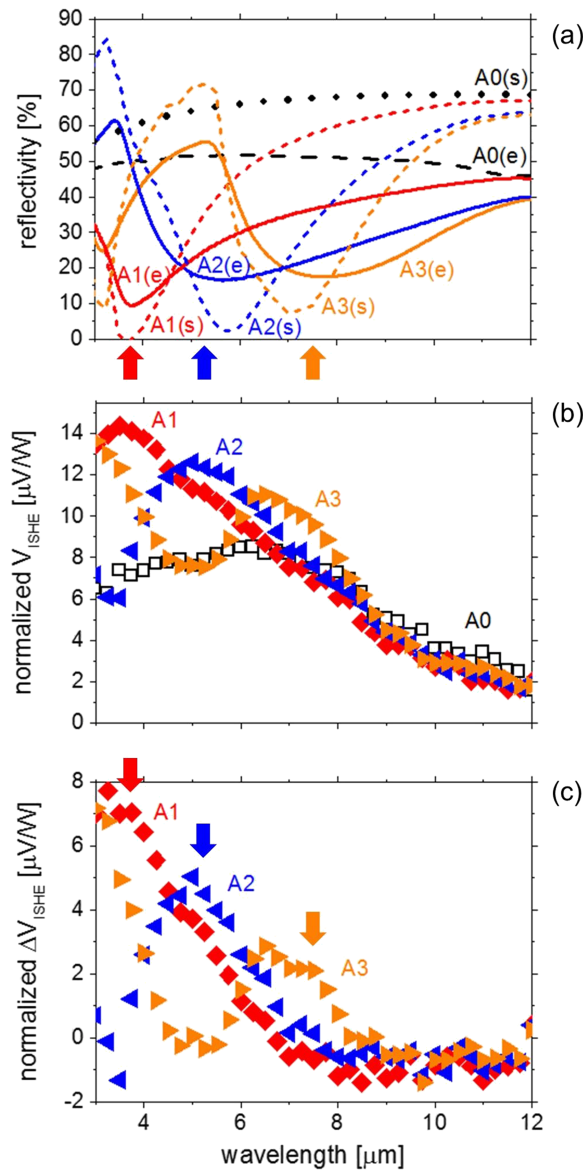


FIG. 5. (a) Measured and simulated reflectivities of the samples where (e) and (s) in the legends indicate measured and simulated reflectivity, respectively. The measurements were done by the FTIR apparatus. The arrows indicate the dips of the measured reflectivities. (b) Measured ISHE voltage ( $V_{\text{ISHE}}$ ) and (c) voltage difference ( $\Delta V_{\text{ISHE}}$ ) between each MIM sample and sample A0. Both of the data are normalized to the power of the incident IR light. In sub-panel (c), the arrows indicate the peak positions which match to the reflectivity dips shown in sub-panel (a).

laser power in the mid-IR was on the order of a few mW, and the repetition rate was fixed at 1 kHz. The laser beam, of diameter of  $\sim 3$  mm, was normally incident at the center of the sample. During the laser irradiation, an external magnetic field was applied along the  $x$  direction unless otherwise specified by an electromagnet, and the induced voltage in the Pt layer along the  $y$  direction was recorded by a nanovoltmeter (2182A, Keithley) (see Fig. 1). The magnetic field was swept between  $-500$  Oe and  $+500$  Oe.

A typical raw data of the output voltage against the applied magnetic field are plotted in Fig. S2 of the [supplementary material](#) for sample A1 at  $4.0 \mu\text{m}$ . Whereas a clear response was observed when the magnetic field is applied along the  $x$  axis, no measurable voltage was generated when the magnetic field was applied along the  $y$  axis [see Fig. S2(b) of the [supplementary material](#)]. This magnetic field dependence is a key feature of the ISHE voltage induced by the PSV effect and the LSSE.

As shown in Fig. S2(a) of the [supplementary material](#), the output voltage saturates when the magnitude of the magnetic field exceeds  $\sim 100$  Oe. Hence, when plotting the  $V_{\text{ISHE}}$  induced by ISHE, one half of the difference in the output voltage at  $+250$  Oe and  $-250$  Oe is used. Similar measurements were repeated by sweeping the incident wavelength from  $2.5 \mu\text{m}$  to  $12.0 \mu\text{m}$  and are summarized in Fig. 5(b). In Fig. 5(b),  $V_{\text{ISHE}}$  was normalized to the laser power, which was wavelength-dependent.

All the samples share the same moderate wavelength dependence as sample A0. Nevertheless, there is a peak in each plot that matches to the dip position in the reflectivity plot of Fig. 5(a). In order to make the peaks originating from the MIM disk more apparent, the  $V_{\text{ISHE}}$  for sample A0 was subtracted from each dataset obtained for samples A1–A3. The resulting  $\Delta V_{\text{ISHE}}$  is plotted in Fig. 5(c). All three samples show definite peaks at the same wavelengths as the reflection minima. These results provide direct evidence of the generation of a wavelength-selective  $V_{\text{ISHE}}$  in the plasmonic absorbers.

#### IV. DISCUSSION

Finally, we discuss the wavelength dependence of sample A0 in terms of  $V_{\text{ISHE}}$ . According to the multiphysics simulations presented in Figs. 2(c) and 3(b), the wavelength dependence of the temperature difference induced by the laser heating is small. This can be explained from the nearly constant absorptivity displayed by sample A0 as shown in Fig. 2(a). Nevertheless, the  $V_{\text{ISHE}}$  for sample A0 has wavelength dependence, with  $V_{\text{ISHE}}$  decreasing at longer wavelengths. We anticipate that this feature is originating mainly from the PSV effect because heating should have little wavelength dependence. Importantly, the ISHE voltage with the peak in samples A1–A3 also exhibit wavelength dependence as seen in Fig. 5(c); although the magnitude of the temperature increase at the resonance wavelength due to the plasmonic absorber has weak wavelength dependence [see Figs. 2(c) and 3(b)], the ISHE enhancement at the resonance condition monotonically decreases with increasing the wavelength. This result suggests that the plasmonic absorbers could have modulated not only the LSSE but also the PSV effect. Separations and optimization of the two effects in plasmonic absorbers to maximize the output spin currents will be the subject of further work.

#### V. SUMMARY

To summarize, we experimentally demonstrated wavelength-selective generation of a spin current using the mid-IR plasmonic absorbers where the spin current was measured using the ISHE. The wavelength that maximizes the spin current can be readily tuned by changing the geometrical parameters of the resonant plasmonic absorbers. The origin of the measured spin current is attributed to both the LSSE and the PSV effect. Plasmonic absorbers allow the subwavelength confinement of light and the localization of heat generation, making them convenient and attractive structures to connect nanophotonics and spintronics.

#### SUPPLEMENTARY MATERIAL

See [supplementary material](#) for the supporting content.

#### ACKNOWLEDGMENTS

The authors thank H. Adachi, S. Kubo, and K. Ikeda for valuable discussions. This work was supported by PRESTO “Phase Interfaces for Highly Efficient Energy Utilization” (JPMJPR12C1), CREST “Phase Interface Science for Highly Efficient Energy Utilization” (JPMJCR13C3), and ERATO “Spin Quantum Rectification” (JPMJER1402) from JST, Japan, Grant-in-Aid for Scientific Research (S) (No. JP16H06364), Grant-in-Aid for Scientific Research (A) (No. JP15H02012), Grant-in-Aid for Encouragement of Young Scientists (A) (No. 17H04801), Grant-in-Aid for Scientific Research on Innovative Area “Nano Spin Conversion Science” (No. JP26103005), Grant-in-Aid for Challenging Research (Exploratory) (No. 17K19045) from JSPS KAKENHI, Japan, NEC Corporation, and the Noguchi Institute.

- <sup>1</sup> S. D. Ganichev, E. L. Ivchenko, V. V. Bel'kov, S. A. Tarasenko, M. Sollinger, D. Weiss, W. Wegscheider, and W. Prettl, "Spin-galvanic effect," *Nature* **417**(6885), 153–156 (2002).
- <sup>2</sup> M. I. Miah, "Observation of the anomalous Hall effect in GaAs," *J. Phys. D: Appl. Phys.* **40**(6), 1659 (2007).
- <sup>3</sup> K. Ando, M. Morikawa, T. Trypiniotis, Y. Fujikawa, C. H. W. Barnes, and E. Saitoh, "Photoinduced inverse spin-Hall effect: Conversion of light-polarization information into electric voltage," *Appl. Phys. Lett.* **96**(8), 082502 (2010).
- <sup>4</sup> C. Leyder, M. Romanelli, J. P. Karr, E. Giacobino, T. C. H. Liew, M. M. Glazov, A. V. Kavokin, G. Malpuech, and A. Bramati, "Observation of the optical spin Hall effect," *Nat. Phys.* **3**(9), 628–631 (2007).
- <sup>5</sup> J. Wunderlich, B.-G. Park, A. C. Irvine, L. P. Zárbo, E. Rozkotová, P. Nemeč, V. Novák, J. Sinova, and T. Jungwirth, "Spin Hall effect transistor," *Science* **330**(6012), 1801–1804 (2010).
- <sup>6</sup> S. Maekawa, S. O. Valenzuela, E. Saitoh, and T. Kimura, *Spin Current* (Oxford University Press, 2012).
- <sup>7</sup> D. Ellsworth, L. Lu, J. Lan, H. Chang, P. Li, Z. Wang, J. Hu, B. Johnson, Y. Bian, J. Xiao, R. Wu, and M. Wu, "Photo-spin-voltaic effect," *Nat. Phys.* **12**(9), 861–866 (2016).
- <sup>8</sup> A. Azevedo, L. H. V. Leão, R. L. Rodríguez-Suarez, A. B. Oliveira, and S. M. Rezende, "dc effect in ferromagnetic resonance: Evidence of the spin-pumping effect?," *J. Appl. Phys.* **97**(10), 10C715 (2005).
- <sup>9</sup> M. V. Costache, M. Sladkov, S. M. Watts, C. H. van der Wal, and B. J. van Wees, "Electrical detection of spin pumping due to the precessing magnetization of a single ferromagnet," *Phys. Rev. Lett.* **97**(21), 216603 (2006).
- <sup>10</sup> E. Saitoh, M. Ueda, H. Miyajima, and G. Tatara, "Conversion of spin current into charge current at room temperature: Inverse spin-Hall effect," *Appl. Phys. Lett.* **88**(18), 182509 (2006).
- <sup>11</sup> S. O. Valenzuela and M. Tinkham, "Direct electronic measurement of the spin Hall effect," *Nature* **442**(7099), 176–179 (2006).
- <sup>12</sup> T. Kimura, Y. Otani, T. Sato, S. Takahashi, and S. Maekawa, "Room-temperature reversible spin Hall effect," *Phys. Rev. Lett.* **98**(15), 156601 (2007).
- <sup>13</sup> K. Uchida, J. Xiao, H. Adachi, J. Ohe, S. Takahashi, J. Ieda, T. Ota, Y. Kajiwara, H. Umezawa, H. Kawai, G. E. W. Bauer, S. Maekawa, and E. Saitoh, "Spin Seebeck insulator," *Nat. Mater.* **9**(11), 894–897 (2010).
- <sup>14</sup> K. Uchida, H. Adachi, T. Ota, H. Nakayama, S. Maekawa, and E. Saitoh, "Observation of longitudinal spin-Seebeck effect in magnetic insulators," *Appl. Phys. Lett.* **97**(17), 172505 (2010).
- <sup>15</sup> K. Uchida, A. Kirihara, M. Ishida, R. Takahashi, and E. Saitoh, "Local spin-Seebeck effect enabling two-dimensional position sensing," *Jpn. J. Appl. Phys., Part 1* **50**(12R), 120211 (2011).
- <sup>16</sup> M. Weiler, M. Althammer, F. D. Czeschka, H. Huebl, M. S. Wagner, M. Opel, I.-M. Imort, G. Reiss, A. Thomas, R. Gross, and S. T. B. Goennenwein, "Local charge and spin currents in magnetothermal landscapes," *Phys. Rev. Lett.* **108**(10), 106602 (2012).
- <sup>17</sup> P. Li, D. Ellsworth, H. Chang, P. Janantha, D. Richardson, F. Shah, P. Phillips, T. Vijayarathy, and M. Wu, "Generation of pure spin currents via spin Seebeck effect in self-biased hexagonal ferrite thin films," *Appl. Phys. Lett.* **105**(24), 242412 (2014).
- <sup>18</sup> M. Agrawal, V. I. Vasyuchka, A. A. Serga, A. Kirihara, P. Pirro, T. Langner, M. B. Jungfleisch, A. V. Chumak, E. T. Papaioannou, and B. Hillebrands, "Role of bulk-magnon transport in the temporal evolution of the longitudinal spin-Seebeck effect," *Phys. Rev. B* **89**(22), 224414 (2014).
- <sup>19</sup> N. Roschewsky, M. Schreier, A. Kamra, F. Schade, K. Ganzhorn, S. Meyer, H. Huebl, S. Geprägs, R. Gross, and S. T. B. Goennenwein, "Time resolved spin Seebeck effect experiments," *Appl. Phys. Lett.* **104**(20), 202410 (2014).
- <sup>20</sup> J. Hao, J. Wang, X. Liu, W. J. Padilla, L. Zhou, and M. Qiu, "High performance optical absorber based on a plasmonic metamaterial," *Appl. Phys. Lett.* **96**(25), 251104 (2010).
- <sup>21</sup> X. Liu, T. Starr, A. F. Starr, and W. J. Padilla, "Infrared spatial and frequency selective metamaterial with near-unity absorbance," *Phys. Rev. Lett.* **104**(20), 207403 (2010).
- <sup>22</sup> N. Liu, M. Mesch, T. Weiss, M. Hentschel, and H. Giessen, "Infrared perfect absorber and its application as plasmonic sensor," *Nano Lett.* **10**(7), 2342–2348 (2010).
- <sup>23</sup> W. Li, U. Guler, N. Kinsey, G. V. Naik, A. Boltasseva, J. Guan, V. M. Shalaev, and A. V. Kildishev, "Refractory plasmonics with titanium nitride: Broadband metamaterial absorber," *Adv. Mater.* **26**(47), 7959–7965 (2014).
- <sup>24</sup> Z. H. Jiang, S. Yun, F. Toor, D. H. Werner, and T. S. Mayer, "Conformal dual-band near-perfectly absorbing mid-infrared metamaterial coating," *ACS Nano* **5**(6), 4641–4647 (2011).
- <sup>25</sup> X. Fang, M. L. Tseng, D. P. Tsai, and N. I. Zheludev, "Coherent excitation-selective spectroscopy of multipole resonances," *Phys. Rev. Appl.* **5**(1), 014010 (2016).
- <sup>26</sup> P. C. Wu, C. Y. Liao, J.-W. Chen, and D. P. Tsai, "Isotropic absorption and sensor of vertical split-ring resonator," *Adv. Opt. Mater.* **5**(2), 1600581 (2017).
- <sup>27</sup> K. Chen, R. Adato, and H. Altug, "Dual-band perfect absorber for multispectral plasmon-enhanced infrared spectroscopy," *ACS Nano* **6**(9), 7998–8006 (2012).
- <sup>28</sup> K. Chen, T. D. Dao, S. Ishii, M. Aono, and T. Nagao, "Infrared aluminum metamaterial perfect absorbers for plasmon-enhanced infrared spectroscopy," *Adv. Funct. Mater.* **25**(42), 6637–6643 (2015).
- <sup>29</sup> W. Li and J. Valentine, "Metamaterial perfect absorber based hot electron photodetection," *Nano Lett.* **14**(6), 3510–3514 (2014).
- <sup>30</sup> X. Liu, T. Tyler, T. Starr, A. F. Starr, N. M. Jokerst, and W. J. Padilla, "Taming the blackbody with infrared metamaterials as selective thermal emitters," *Phys. Rev. Lett.* **107**(4), 045901 (2011).
- <sup>31</sup> T. D. Dao, K. Chen, S. Ishii, A. Ohi, T. Nabatame, M. Kitajima, and T. Nagao, "Infrared perfect absorbers fabricated by colloidal mask etching of Al–Al<sub>2</sub>O<sub>3</sub>–Al trilayers," *ACS Photonics* **2**(7), 964–970 (2015).
- <sup>32</sup> T. Yokoyama, T. D. Dao, K. Chen, S. Ishii, R. P. Sugavaneshwar, M. Kitajima, and T. Nagao, "Spectrally selective mid-infrared thermal emission from molybdenum plasmonic metamaterial operated up to 1000 °C," *Adv. Opt. Mater.* **4**(12), 1987–1992 (2016).

- <sup>33</sup> T. D. Dao, S. Ishii, T. Yokoyama, T. Sawada, R. P. Sugavaneshwar, K. Chen, Y. Wada, T. Nabatame, and T. Nagao, "Hole array perfect absorbers for spectrally selective mid-wavelength infrared pyroelectric detectors," *ACS Photonics* **3**(7), 1271–1278 (2016).
- <sup>34</sup> K. Uchida, H. Adachi, D. Kikuchi, S. Ito, Z. Qiu, S. Maekawa, and E. Saitoh, "Generation of spin currents by surface plasmon resonance," *Nat. Commun.* **6**, 5910 (2015).
- <sup>35</sup> K. Uchida, H. Adachi, T. Kikkawa, A. Kirihara, M. Ishida, S. Yorozu, S. Maekawa, and E. Saitoh, "Thermoelectric generation based on spin Seebeck effects," *Proc. IEEE* **104**, 1499 (2016).
- <sup>36</sup> A. D. Rakić, A. B. Djurišić, J. M. Elazar, and M. L. Majewski, "Optical properties of metallic films for vertical-cavity optoelectronic devices," *Appl. Opt.* **37**(22), 5271–5283 (1998).
- <sup>37</sup> M. Schreier, A. Kamra, M. Weiler, J. Xiao, G. E. Bauer, R. Gross, and S. T. Goennenwein, "Magnon, phonon, and electron temperature profiles and the spin Seebeck effect in magnetic insulator/normal metal hybrid structures," *Phys. Rev. B* **88**(9), 094410 (2013).